Journal of the European Ceramic Society 43 (2023) 6493–6503

Contents lists available at ScienceDirect

Journal of the European Ceramic Society

journal homepage: www.elsevier.com/locate/jeurceramsoc

Evaluating the suitability of fast sintering techniques for the consolidation of calcium phosphate scaffolds produced by DLP

Claudia Paredes [a,b,*], Jakub Roleček [b], Lucie Pejchalová [b], Tomáš Spusta [b], David Salamon [b], Pedro Miranda [a]

[a] Departamento de Ingeniería Mecánica, Energética y de los Materiales, Universidad de Extremadura, Badajoz, Spain
[b] Central European Institute of Technology, Brno University of Technology, Brno, Czech Republic

ARTICLE INFO

Keywords:
Scaffolds
Calcium phosphate
Mechanical properties
Digital Light Processing
Spark Plasma Sintering

ABSTRACT

Porous scaffolds were fabricated via Digital Light Processing (DLP) from β-TCP powder and sintered by conventional sintering in air *(CSA)*, rapid sintering in air *(RSA)* and pressure-less spark plasma sintering in vacuum *(pl-SPS)*, at four different temperatures: 1200, 1300, 1400 and 1500 ºC. Each sintering strategy resulted in scaffolds with different phase composition, microstructure and mechanical properties. Long dwell times or high temperatures were required to achieve a complete β→α transformation, and rapid cooling rates avoided the reverse transformation. The presence of graphite in the sintering chamber played a crucial role in stabilising the α-TCP phase, phase prevailing in SPS-treated scaffolds, hindered their densification and avoided the generation of transformation-induced cracks. All scaffolds exhibited compressive strengths within the range of cancellous bone, with the highest average value of 22 ± 4 MPa achieved by the *RSA* scaffolds sintered at 1300 ºC, thanks to their greater densification and fine microstructure.

1. Introduction

The excellent osteoconductivity and bioactive properties of tricalcium phosphates (TCP) have promoted their use as bone cements and substitutes in therapeutic repair procedures based on bone tissue engineering [1]. This material can be found in several allotropic forms, but only two phases are stable/metastable at room temperature. The most stable polymorph is β, which undergoes a phase transformation to α above 1135 °C [2]. While β-TCP exhibits excellent biomineralisation and cell adhesion, α-TCP shows higher solubility and transforms into calcium-deficient hydroxyapatite in a biological environment [2,3]. The greatest disadvantages of calcium phosphates are their brittleness and lower strength, a combination that limits their use as bone implants in load-bearing regions of the skeleton. Due to the difficulty of sintering α-TCP [2,4], this polymorph has mainly been used in the development of bioactive pastes or cements for bone repair, while defect-free dense bodies made from α-TCP have not been widely reported. Therefore, their mechanical properties have not been extensively studied and to date only a few studies have addressed the fabrication of α-TCP dense scaffolds [4].

Using Additive Manufacturing (AM), in particular Digital Light Processing (DLP), it is possible to create patient-specific bone scaffolds with customised biodegradable properties and simultaneously improve the mechanical properties of these lattices while preserving pore interconnectivity throughout the structure [5,6]. Like other vat polymerisation processes, DLP enables the manufacturing of complex 3D objects layer by layer, using UV light to selectively harden a liquid photopolymeric resin. In the case of TCP parts, a suspension is created by adding ceramic powder to the photopolymer resin. Similarly, the photo-curing suspension is loaded on a transparent vat onto which the printer projects sequential images corresponding to the layers into which the object has previously been divided. As the resin cures to a predetermined thickness, the ceramic particles are trapped in the hardened layer [7–9]. Subsequently, a debinding process is necessary to remove the organic material before sintering the resulting calcium phosphate body.

During sintering, the ceramic particles join together to constitute a solid body through diffusion. With conventional heating densification of TCP is often achieved at the expense of enormous grain growth and the formation of cracks due to the volumetric changes that occur during TCP phase transformations. Both the uncontrolled grain growth and the transformation-induced cracking reduce the mechanical performance of

* Corresponding author at: Departamento de Ingeniería Mecánica, Energética y de los Materiales, Universidad de Extremadura, Badajoz, Spain.
E-mail address: clparedes89@unex.es (C. Paredes).

https://doi.org/10.1016/j.jeurceramsoc.2023.05.052
Received 20 March 2023; Received in revised form 31 May 2023; Accepted 31 May 2023
Available online 1 June 2023

the sintered bodies [10,11]. Although several recent studies have addressed the sintering of calcium phosphates by advanced sintering techniques [10,12,13], their applicability to laminar structures of calcium phosphates deposited by DLP remains untested. Only a few studies have succeeded in sintering complex porous objects without the use of pressure [14], and not always maintaining a small grain size or preventing the formation of cracks.

This study aims to analyse the sintering behaviour of tricalcium phosphate scaffolds fabricated by DLP using rapid sintering techniques at different temperatures. In particular, the scaffolds will be sintered using conventional sintering in air (*CSA*), rapid sintering in air (*RSA*), and pressure-less spark plasma sintering in vacuum (*pl-SPS*) at 1200, 1300, 1400 and 1500 ºC, with different heating regimes. Therefore, it will be studied how different heating rates, dwell times and sintering atmospheres influence their phase composition, microstructure and compressive strength. The resulting scaffolds will be compared to identify the best strategy to obtain bioactive scaffolds with a dense microstructure while maintaining a small grain size and a tailored phase composition, in order to improve their mechanical performance and bioactivity while reducing processing times.

2. Materials and methods

2.1. Fabrication

Photosensitive ceramic suspensions with a solid loading of 40 vol% were created using the following formulation, developed in a previous study [15]: commercially available β-TCP powder (Whitlockite OD, Plasma Biotal Limited, United Kingdom), with an average particle size of 2.36 μm, and a density of 3.07 g/cm^3, was coated with 0.1 wt% of oleic acid (OA) in order to avoid sedimentation [16,17]. This powder was added to an unpigmented acrylic resin (FTD Standard Blend 3D Printing resin, Fun to Do, Netherland), with a density of 1.13 g/cm^3 and a viscosity of 0.07 Pa·s (at a shear rate of 10 s^{-1}), in which a 30 wt% of camphor was previously diluted in order to reduce its viscosity and facilitate printing [18]. All the components were then mixed in a centrifugal planetary mixer THINKY ARE-250 (THINKY, Japan) and the suspension was stored at a temperature of approximately 37 °C to facilitate flowability during printing [19].

Cubic-shaped porous scaffolds with external dimensions of 6.0 × 6.0 × 6.0 mm were created by 3D modelling. They consisted of 4 layers of square section struts crossing at common points in the three orthogonal directions of the space. Specifically, the designed strut thickness was t = 0.6 mm, separated a distance s = 1.2 mm, both horizontally and vertically. This arrangement corresponded to a porosity of 64.8% of their total volume.

The green bodies were obtained using the DLP bottom-up fabrication system Asiga Max Mini UV385 (Asiga, Australia). For this purpose, the 3D models were sliced into 50 μm thick layers and the suspension was loaded onto a transparent vat. Polymerisation of each layer was induced by exposing the suspension for 0.252 s to UV light radiation at a wavelength of 385 nm and an intensity of 31 mJ/cm^2. Post-processing consisted firstly of the removal of uncured resin residues trapped in the pores using isopropanol, sonication and drying with compressed air, and secondly of a post-curing treatment performed in a UV light chamber for 2 min, which ensures the integrity of the specimens and reduces the likelihood of delamination or other deformation defects appearing due to uneven curing.

2.2. Heat treatment

In order to minimise defects caused by the release of gases during the degradation of the cured polymer in air [20,21], and to accelerate the typically long process, a two-step heat treatment was employed for debinding. In the first step, the printed samples were vacuum debinded in a retort furnace (CLASIC 2011DEB, Clasic Ltd., Czech Republic). Based on previous thermogravimetric analysis [15], two ramps of 0.5 °C/min up to 300 °C and 390 °C respectively were used, with dwell times of 60 min at each temperature. For samples that were not to be sintered in air (i.e. SPS-sintered in vacuum), any residual carbon present in the samples after this initial oxygen-free debinding treatment, was eliminated in a second step in a conventional furnace (CLASIC 1200 M, Clasic Ltd., Czech Republic) at 750 °C for an hour using a heating rate of 1 °C/min.

Conventional and advanced sintering methods were compared at four different temperatures: 1200, 1300, 1400 and 1500 °C, as summarised in Table 1. Thus, batches of 10 samples were sintered by conventional sintering in air (***CSA***), rapid sintering in air (***RSA***) or pressure-less Spark Plasma Sintering in vacuum (***pl-SPS***) at each temperature. *CSA* was performed in a conventional chamber furnace (CLASIC 1800 C, Clasic Ltd., Czech Republic) using heating rates of 3 °C/min, dwell times of 120 min and cooling rates of 10 °C/min. The samples collected after sintering were marked as ***CSA-1200, CSA-1300, CSA-1400*** and ***CSA-1500***, according to the sintering temperature.

On the other hand, *RSA* was carried out in a furnace with a bottom loading mechanism (CLASIC 0117E, Clasic Ltd., Czech Republic). This furnace allowed to controllably insert the sample holder into the hot zone, located in its upper part, at a pre-set heating rate that is controlled by the speed of the platform movement (see Fig. 1a). Heating and cooling rates of 100 °C/min were employed with a dwell time of 5 min at the selected temperature, which was controlled by a thermocouple located near the samples. As before, the sintered samples were marked as ***RSA-1200, RSA-1300, RSA-1400*** and ***RSA-1500***, according to their sintering temperature.

The same heating and cooling rates as for *RSA* were used to sinter the scaffolds in the SPS apparatus (SPS-625, Dr. Sinter, Japan). Although in this case the process was performed in a mild vacuum (i.e., <10 Pa), no direct mechanical force was applied to the samples as in the previous cases to facilitate comparison. For this purpose, the scaffolds were placed in a covered graphite crucible with an inner diameter of 50 mm and a height of 20 mm. A pulsed DC current was circulated through the crucible with a duty cycle of 12 ms ON / 2 ms OFF in order to generate the heat, and a minimal compression load (~1.5 kN) was induced on the crucible to ensure good electrical contact (see Fig. 1b). Throughout the process, the temperature of the system was monitored by a radiation thermometer focused on the inner surface of the crucible through a small hole drilled in its wall. Again, the sintered samples were marked according to the selected treatment as ***SPS-1200, SPS-1300, SPS-1400*** and ***SPS-1500***.

In addition, in order to isolate the effect of the sintering atmosphere on the scaffold's final density, some specimens were sintered in a conventional furnace (Xerion furnace, Xerion Berlin Laboratories GmbH, Germany) and a gas pressure furnace (CLASIC Graphite Pressure Furnace, Clasic Ltd., Czech Republic) using three different atmospheres (air, vacuum, and nitrogen) and the same regime (heating ramp of 3 °C/min up to 1200 °C and a dwell time of 120 min) as for the *CSA* samples.

2.3. Microstructural characterisation

To evaluate and compare the densification achieved by each sintering treatment, the apparent density and the shrinkage of the specimens

Table 1
Heat treatment used in conventional sintering in air (CSA), rapid sintering in air (RSA) and pressure-less Spark Plasma Sintering (pl-SPS) at 1200, 1300, 1400 and 1500 °C.

	CSA	*RSA*	*pl-SPS*
Atmosphere	Air	Air	Vacuum
Heating rate	3 °C/min	100 °C/min	100 °C/min
Dwell time	120 min	5 min	5 min
Cooling rate	10 °C/min	100 °C/min	100 °C/min

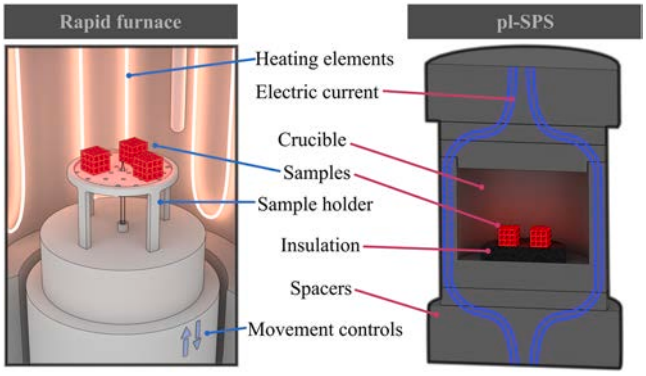

Fig. 1. Schematic of scaffolds heat treatment in (a) the Rapid Sintering furnace with bottom loading mechanism and (b) pressure-less Spark Plasma Sintering apparatus.

were determined by measuring their weight and external dimensions using a digital balance and calliper. Scanning electron microscopy (S3600 N, Hitachi, Japan; Verios 460 L, Thermo Fisher Scientific Brno s. r.o., Czech Republic and TESCAN LYRA3, TESCAN Brno, s.r.o., Czech Republic) was performed to reveal the scaffold's struts shape, surface quality and microstructure, as well as to estimate their grain size and porosity. Average grain size values were obtained by Gauss fitting, for which more than 400 grains were measured. As phase transformations were expected to occur during sintering at the selected temperatures [22–24], the crystalline phases present in the samples were also identified by X-ray diffractometry (XRD, Rigaku SmartLab 3 kW) on powder obtained by crushing the sintered specimens. Diffractometries were performed at 40 kV voltage and 30 mA current, in Bragg-Brentano measurement mode between 10º and 90º with a scan speed of 3º/min. A Rietveld's refinement was applied to all XRD patterns using MAUD (Material Analysis Using Diffraction) software [25]. The structural models corresponding to α-TCP and β-TCP [26–28] published in the Crystallography Open Database were employed to estimate the quantity of each phase using the mentioned software.

2.4. Mechanical testing

The compressive strength (σ_c) of the sintered specimens was determined from the maximum stress recorded during uniaxial compression tests. These tests were performed on a universal testing machine (Shimadzu Autograph AG-IS, Japan) in air. The load was applied perpendicular to the building plane at a constant crosshead speed of 0.6 mm/min. Nominal stress–strain curves were obtained by normalising the captured load vs. displacement data using the initial external dimensions of each sample. Batches of minimum 6 specimens per sintering condition were tested.

3. Results and discussion

3.1. Microstructural characterisation

SEM micrographs corresponding to the lateral surface of representative sintered scaffolds for all temperatures and methods (*CSA*, *RSA* and *pl-SPS*) are displayed in Fig. 2, as labelled. A vertical strut is shown at larger magnification, with the full specimen as an inset, both oriented with the first printed layer at the bottom. While scaffolds sintered by *pl-SPS* exhibit a regular cubic shape regardless of the sintering temperature used, pictures corresponding to *CSA* and *RSA* scaffolds show that the specimens suffer significant distortions when heated above 1200 °C. Indeed, especially in the case of *CSA*, scaffolds sintered at 1300 and 1400 °C tended to adopt an elephant's foot shape, revealing an uneven densification between their top and bottom parts. This could be attributed to the thermal insulation effect of the alumina plate in the case of *CSA* and the alumina foam in the case of *RSA*, on which the scaffolds were supported during sintering, but this situation is unlikely in the case of *CSA*, where a two-hour dwell time should have been sufficient to homogeneously heat the scaffolds from all sides. However, this effect disappeared when scaffolds were sintered at 1500 °C, where uniform densification must have been achieved. When sintering stoichiometric β-TCP above 1288 °C, a liquid phase is expected to form and increase with the temperature [29]. The presence of this liquid phase could then be responsible for the improved densification of these scaffolds.

The external dimensions of the green bodies were 5.97 ± 0.05 mm, very close to the CAD model. These were used to evaluate the shrinkage of the scaffolds after each of the sintering routes. The behaviour of the *CSA* and *RSA* treated specimens was quite similar and their shrinkage increased progressively with increasing temperature. The measured values ranged from 17 ± 2% at 1200 °C to 19 ± 2% at 1500 °C for *CSA* scaffolds, and from 15 ± 1% to 20 ± 3% in *RSA* scaffolds in the same temperature range. On the contrary, minimal variations were measured for the *pl-SPS* scaffolds at the three lower temperatures, with a shrinkage of around 10%, while at 1500 °C the shrinkage increased to 13 ± 1%, still far from the values obtained in *CSA* and *RSA*. This data is summarised together with apparent density measurements for all scaffolds in Table 2.

Despite a generally good surface appearance, as typical of DLP fabrications, it is possible to easily distinguish the individual building layers that comprise the struts on their captured surface. In addition, some delamination and other defects, probably related to the elimination of the organics (indicated by white arrows in Fig. 2), were also identified. Another possible cause of these defects could be related to residual carbon elimination during sintering in *CSA* and, especially, *RSA* specimens, since the high heating rates employed during sintering could lead to uncontrolled gas release [21]. However this is unlikely since the remaining carbon content after vacuum debinding, quantified in previous study [15] to be ~3%, is too low to induce these defects. It should also be noted that the above-mentioned defects were less evident in the scaffolds with a higher degree of densification.

SEM micrographs of the polished and thermally etched surfaces of all sintered scaffolds included in Fig. 3 revealed clear differences in their microstructures.

The specimens that underwent *CSA* and *RSA* treatments exhibited a similar tendency: a visible and progressive reduction in porosity and increase in grain size with the rising sintering temperature, which was much less evident in *pl-SPS* samples. A quantitative comparison of these estimated values of both parameters are included in Fig. 4.

Surface microporosity data in Fig. 4a evidence clear differences between the three sintering methods. At first sight, it is evident that the densities of specimens sintered in air, both *CSA* and especially *RSA*, are clearly higher than those of the *pl-SPS* sintered samples. And while a monotonic decrease in microporosity with temperature is observed in *CSA scaffolds, RSA* and especially *pl-SPS* samples show no significant densification at the higher temperatures. Thus, fast sintering strategies seem to achieve final density at lower temperatures compared to conventional sintering. In fact, *CSA* required a temperature of 1500 °C to achieve a level of microporosity similar to that of *RSA* samples sintered at 1300 °C. This is typically attributed to fast sintering inhibiting grain growth, which in turn facilitates surface diffusion and accelerates densification. This is in good agreement with grain size measurements (Fig. 4b), which were in general significantly lower in the fast sintering processes. However, despite exhibiting the smallest grain sizes at most temperatures, the microporosity of *pl-SPS* samples varied from almost twice that of *RSA* counterparts already at 1200 °C to more than five times higher at 1500 °C, despite both treatments using the same temperature profile. The difference in sintering atmosphere between *RSA* and *pl-SPS* seems the most obvious suspect for these density differences. However, sintering experiments were carried out in a conventional

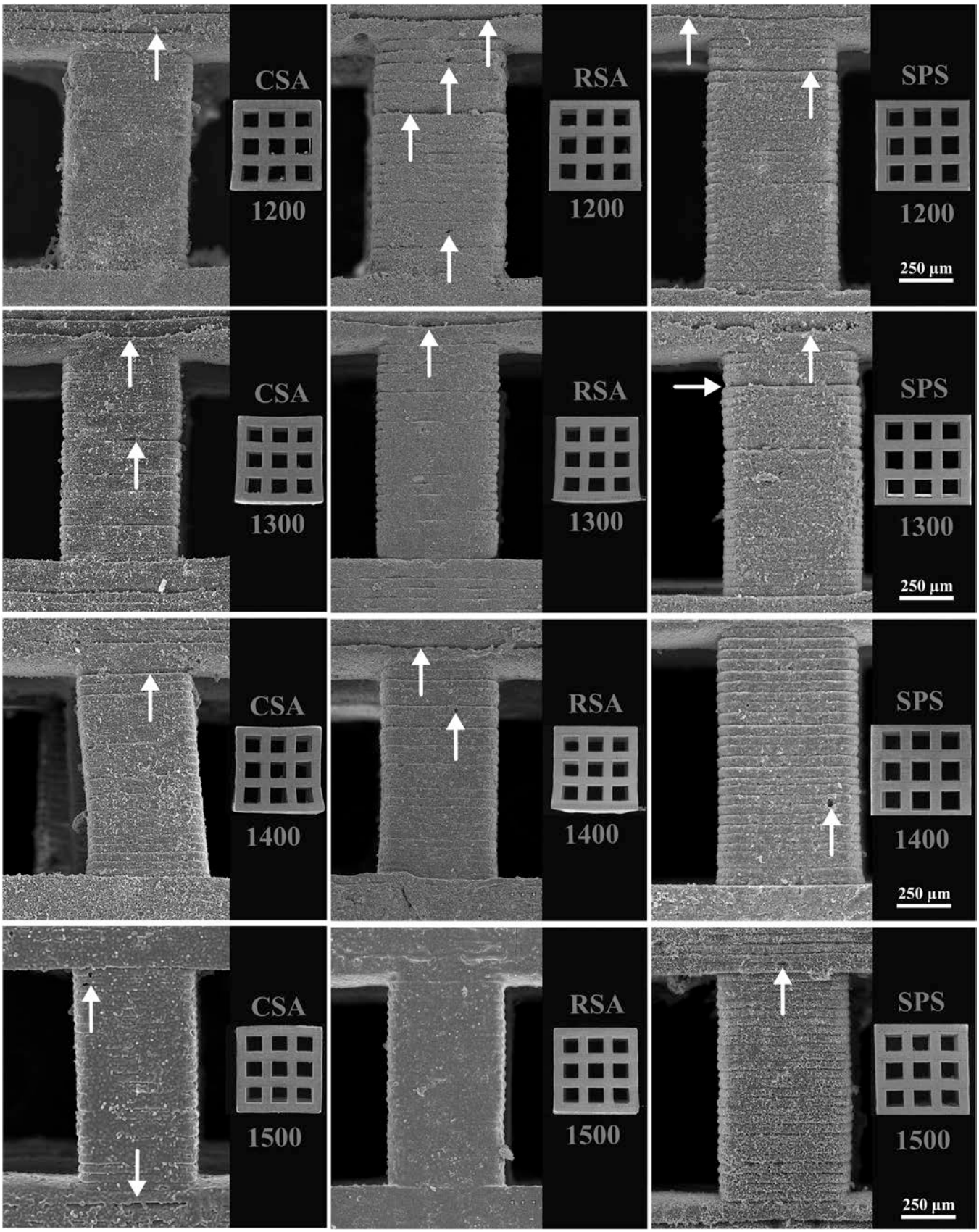

Fig. 2. Representative SEM micrographs of the lateral surface of struts corresponding to scaffolds sintered as indicated on the right insets, which include overall views of the scaffolds. Arrows indicate small defects attributed to the elimination of the organics.

Table 2
Scaffolds' external dimensions and apparent density values.

Sample		External dimensions [mm]	Apparent density [g/cm^3]
Green body		5.97 ± 0.05	-
CSA-	***1200***	4.96 ± 0.08	0.96 ± 0.03
	1300	4.9 ± 0.1	1.01 ± 0.03
	1400	4.8 ± 0.1	1.05 ± 0.05
	1500	4.81 ± 0.08	1.06 ± 0.03
RSA-	***1200***	5.1 ± 0.1	0.94 ± 0.03
	1300	4.79 ± 0.09	1.12 ± 0.04
	1400	4.8 ± 0.1	1.10 ± 0.03
	1500	4.8 ± 0.1	1.11 ± 0.05
pl-SPS-	***1200***	5.32 ± 0.08	0.79 ± 0.03
	1300	5.39 ± 0.04	0.76 ± 0.02
	1400	5.36 ± 0.03	0.79 ± 0.03
	1500	5.18 ± 0.07	0.89 ± 0.03

controlled atmosphere furnace under three different atmospheres (air, nitrogen and vacuum) using the same slow treatment (heating rate of 3 °C/min and a dwell time of 120 min at 1200 °C). The results, which are also included in Fig. 4a as light grey solid squares, indicate that the change in atmosphere only increases densification of the sample, especially under vacuum. Therefore, the vacuum does not explain the poorer densification obtained in the *pl-SPS* treatments. Instead, it is the graphite lining/heating elements used in the *SPS* furnace and the graphite crucibles containing the samples are considered responsible for the observed differences. This was corroborated by using the same slow heating setup but in a gas pressure furnace with graphite lining and heating elements, where samples were sintered under a nitrogen atmosphere and vacuum. The results of these experiments, included in Fig. 4a as hollow squares, evidence that the density achieved by scaffolds sintered in the gas-pressure furnace, regardless of the employed atmosphere, is noticeably lower than in the case of samples sintered in the conventional furnace. Thus, the presence of graphite in the furnace severely hampers densification during sintering, in accordance with previous studies dealing with the sintering of ceramic oxides by SPS [30, 31]. This is probably due to the incorporation of carbon into the TCP microstructure as an interstitial element, explaining the poor performance of the *pl-SPS* sintering treatment.

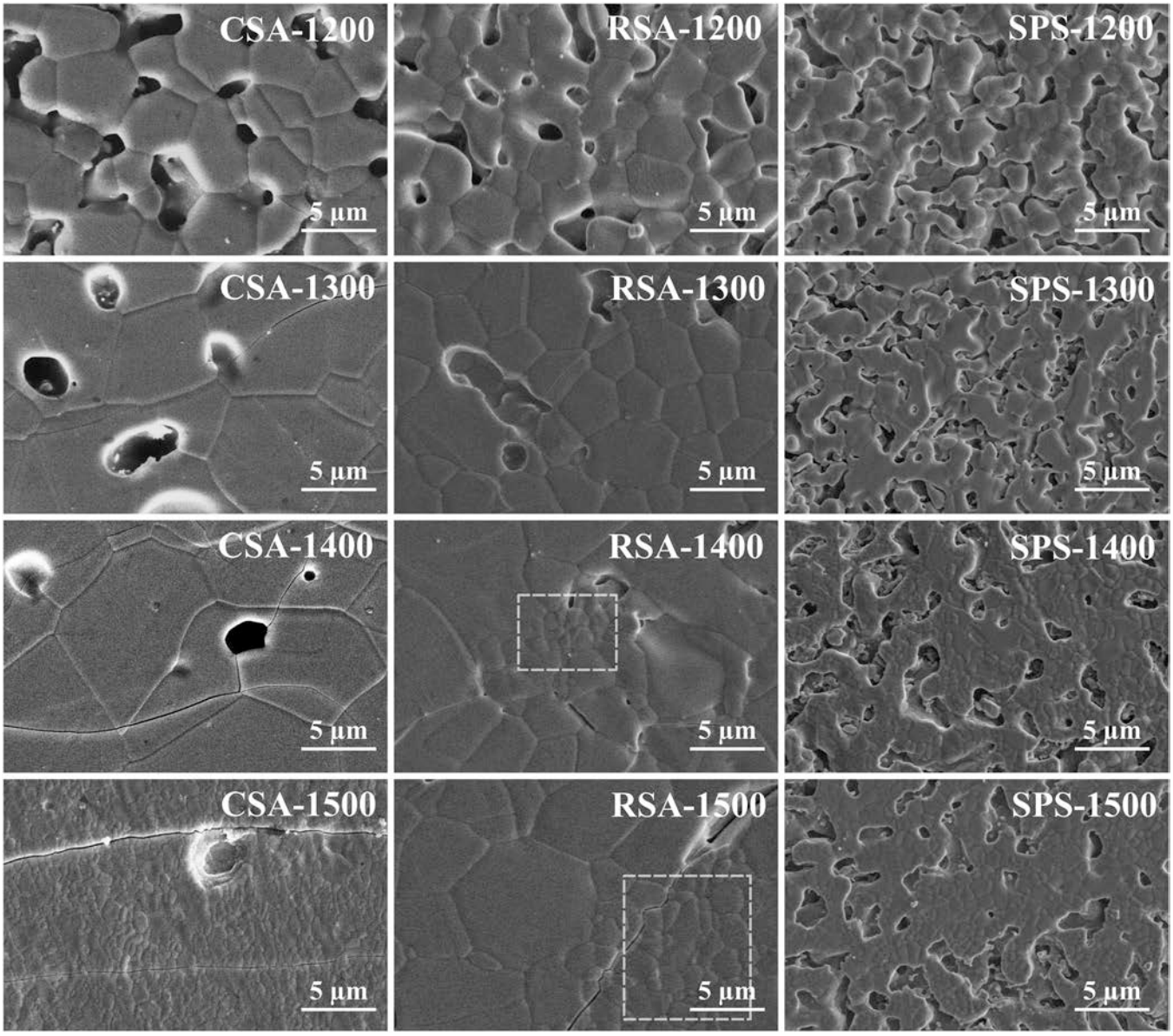

Fig. 3. SEM cross-sectional micrographs of polished and thermally etched surfaces of CSA, RSA and pl-SPS samples sintered at 1200, 1300, 1400 and 1500 °C, as indicated in the legend. Coarse dashed lines indicate the presence of a second phase (corresponding to α-TCP) [29].

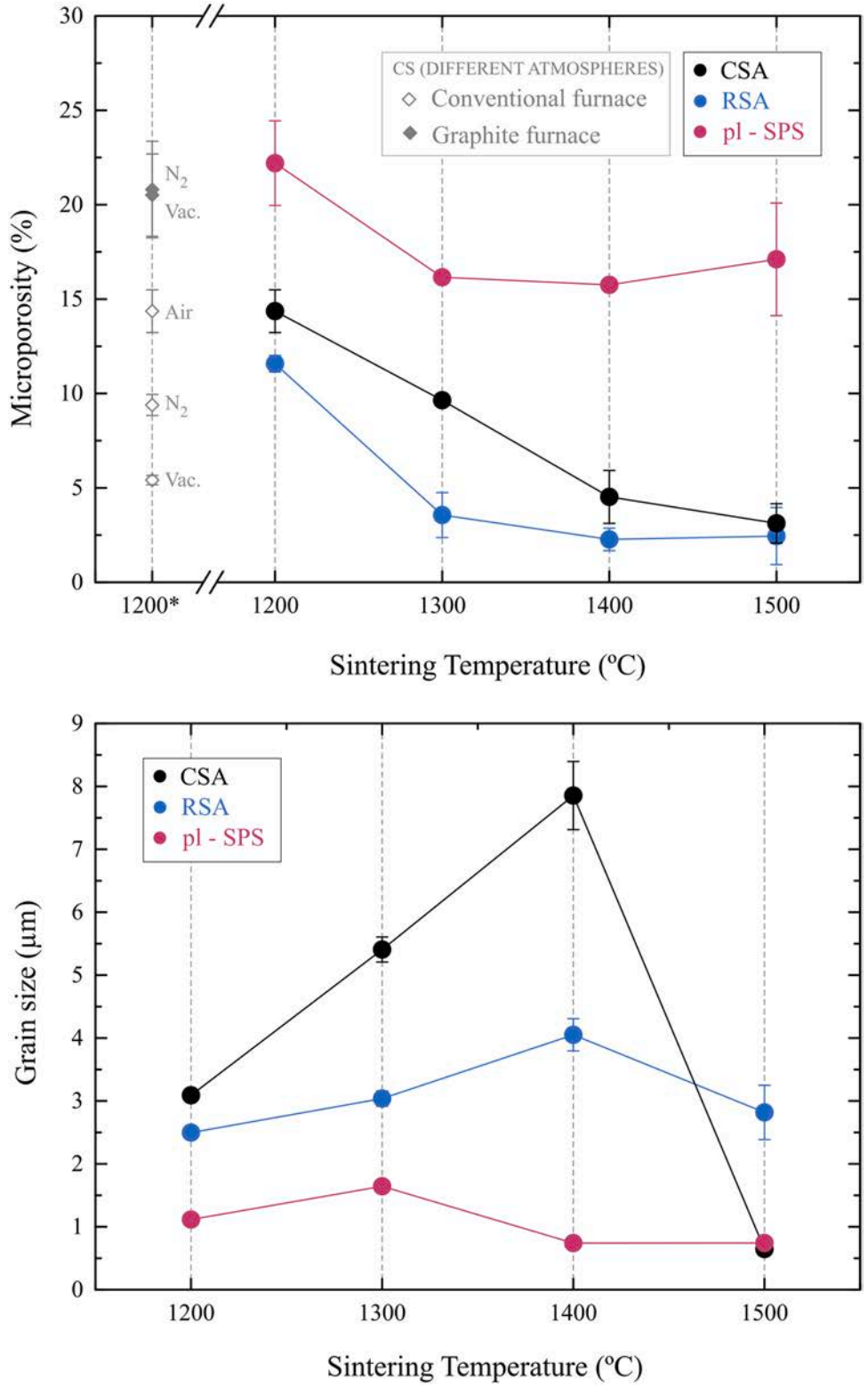

Fig. 4. Plot of (a) surface microporosity and (b) average grain size of scaffolds as a function of the sintering temperature for at each process: conventional furnace in air (CSA), rapid sintering in air (RSA) and SPS apparatus (pl-SPS), as indicated.

Grain size evolution with sintering temperature (Fig. 4b) also warrants additional analysis. Besides the already mentioned reduction in grain growth achieved by rapid sintering treatments—which is already evident in the average grain size values at 1200 °C, and which increases up to a 100% or more difference at higher temperatures—it is worth noting that this growth is interrupted by the appearance of a new phase in the form of aggregates of considerably finer grains. These are quite evident in the microstructure of *RSA-1400* and *RSA-1500* scaffolds (Fig. 3). These fine grains also dominate the microstructure of the *CSA* samples sintered at 1500 °C. This means that *CSA* scaffolds sintered at this temperature have an average grain size almost five times smaller than their *RSA* counterparts, as shown in Fig. 4b. Similar reductions in

grain size could be observed in *pl-SPS* samples sintered at 1400 °C or above.

The XRD patterns of sintered scaffolds shown in Fig. 5 confirm the occurrence of a permanent phase transformation at the higher sintering temperatures. The starting ceramic powder consisted of pure β-TCP, which was the only crystalline phase identified in all sintered scaffolds up to 1200 °C, regardless of the sintering technique. However, the high temperature polymorph of the material (α-TCP) was found in scaffolds sintered at higher temperatures. As already mentioned, the relative amounts of each phase were quantified through a Rietveld phase fraction analysis using MAUD software. Convergence was reached in the refinement of all patterns and quantitative estimations of both phases were confirmed by a residual in weight (R_{wp}) ranging from 4% to 9%, and a significance level lower than 0.04. It is important to note that Rietveld refinement of β-TCP XRD data using published crystal structures often leaves some systematic mismatches due to different factors [32] which prevents a perfect fit.

While *CSA* scaffolds sintered at 1300 °C still consisted of pure of

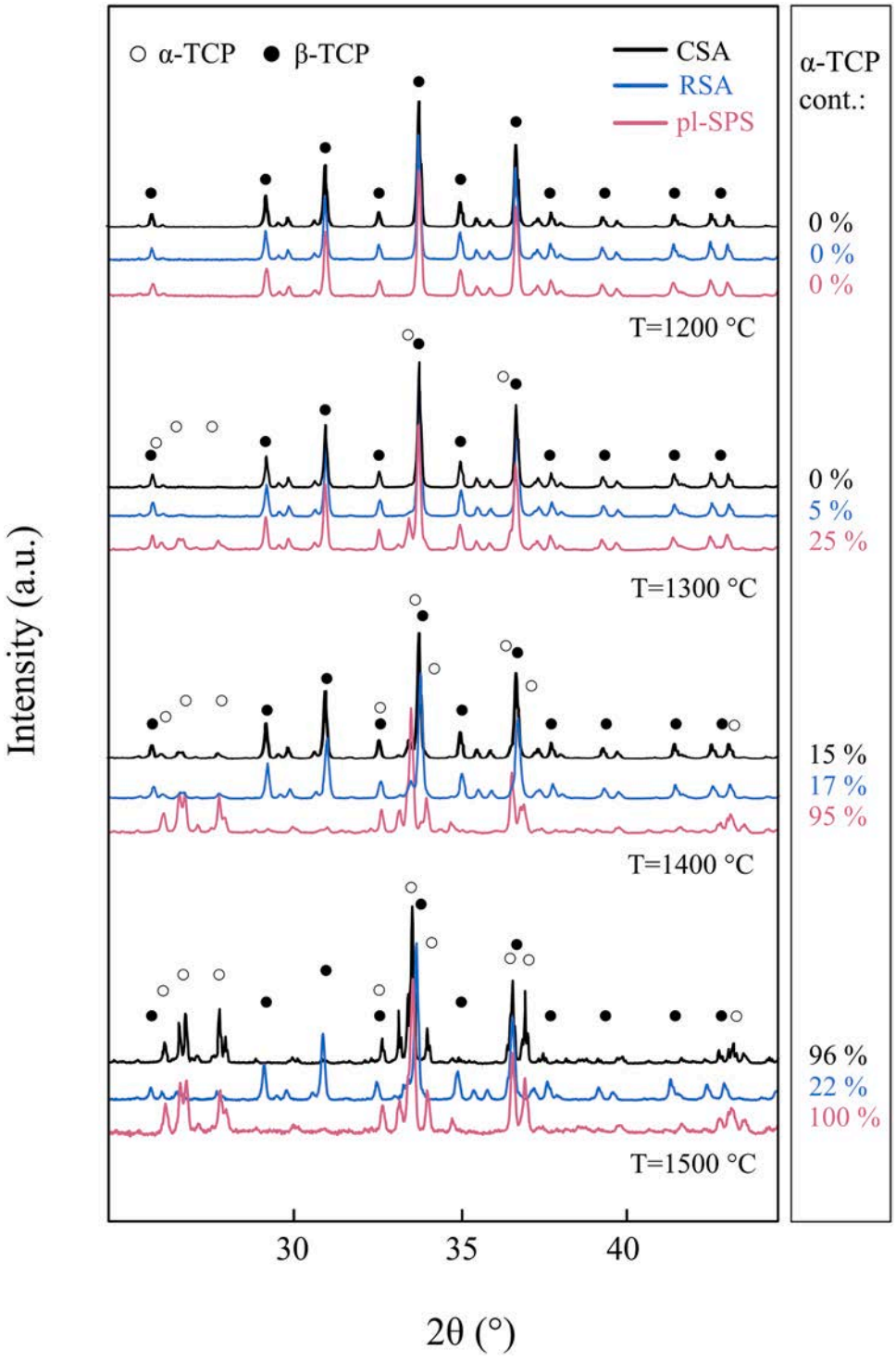

Fig. 5. XRD patterns of CSA, RSA and pl-SPS scaffolds sintered at 1200 °C, 1300 °C, 1400 °C and 1500 °C, as indicated. Main peaks of the identified crystalline phases are labelled with symbols according to the legend, and the content (wt%) of α-TCP phase estimated from Rietveld analyses is shown on the right.

β-TCP, significant fractions of α-TCP of 5% and 25% were present in *RSA* and *pl-SPS* scaffolds, respectively. Both phases were also present in samples sintered at 1400 °C. In *CSA* and *RSA* scaffolds sintered at this temperature, fractions of approximately 15% and 17% of α-TCP were found, respectively, while it was almost the only phase present (95%) in *pl-SPS* scaffolds. Finally, at 1500 °C pure α-TCP was obtained in *pl-SPS* scaffolds and also almost (96%) in *CSA* structures, while β-TCP remained the primary phase (78%) present in *RSA* scaffolds.

A phase transformation (β→α) is known to occur in TCP at temperatures over 1115–1160 °C [32,33]. Therefore, it is likely that during the two-hour dwell time employed in the conventional furnace, a significant portion of the original β-TCP underwent transformation to α-TCP at all the analysed temperatures. However, it was not unexpected to find β-TCP in all the *CSA* samples, since the reverse transformation (α→β) can occur during cooling, especially when slow cooling rates are used [32,33]. Although the same cooling rate was employed for all sintering temperatures, the fraction of β-TCP in the samples noticeably decreased with increasing sintering temperatures, to the point that *CSA-1500* samples were predominantly composed of α-TCP. This indicates that the two hour dwell time at lower temperatures was probably not sufficient to reach equilibrium (transformation of all β-TCP to α-phase) and therefore a lower fraction of α-phase was retained after the reverse transformation [33–35].

On the other hand, the dwell time employed in the case of *RSA* scaffolds was considerably shorter than that used for sintering *CSA* scaffolds (5 min vs. 120 min), and therefore an even smaller amount of material would be expected to undergo the phase transformation to α-TCP. Despite that, *RSA-1300* an *RSA-1400* scaffolds contained a slightly higher amount of α-TCP than their *CSA* counterparts. This is explained by the rapid cooling rates used in the rapid furnace, which limited the reverse transformation. Additional *RSA* treatments performed at 1400 °C with the same dwell time and cooling rate as *CSA* yielded the same final α-TCP content (14%) as *CSA* treatments, while the same treatments with a rapid cooling rate of 100 °C/min yielded 54% α-TCP content. These results confirm, on the one hand, the critical role of the cooling rate in the retention of the high-temperature phase and, on the other hand, the need for long dwell times to achieve the β→α transformation, since this latter α content was much higher than that obtained in the original *RSA* treatments (17%).

Interestingly, *pl-SPS* scaffolds exhibited even higher fractions of α-TCP than *RSA* scaffolds at all temperatures (Fig. 5), even though dwell times and heating/cooling rates were the same. This result indicates that the chemical environment during sintering plays a very important role in the final phase composition of the scaffold as well. In particular, as discussed regarding grain size, the presence of graphite in the furnace chamber is more critical than the sintering atmosphere itself. In fact, carbon can be interstitially incorporated into the TCP crystal structure, stabilising the more open crystal structure of its α-phase. This simultaneously promotes the β→α phase transformation at high temperature and hampers the reverse transformation to the denser β phase during cooling. This was verified by performing sintering treatments in a gas pressure furnace with graphite heating elements, using the same heating sequence as in *CSA*, which yielded almost pure (97%) α-TCP samples already at 1300 °C (as opposed to the 1500 °C required in *CSA*), regardless of the sintering atmosphere (vacuum or nitrogen) employed.

TCP phase transformations, whether reversible or not, involve significant volumetric changes in the crystal lattice [11,34], which generate important internal stresses in the material, often leading to microcracking. It is therefore not surprising that these cracks already appeared in the *CSA-1300* specimens (Fig. 3) and their number and size increased at higher temperatures in both air furnaces, regardless of dwell time and heating/cooling rates. However, in the *pl-SPS* treated scaffolds, there is a clear reduction in the level of microcracking observed compared to their *RSA/CSA* counterparts. These differences could be attributed to the reduced occurrence of the reverse transformation, but are most likely related to the reduction of the stresses associated with the phase transformation as a consequence of their lower densification and/or the compressive stresses introduced by the presence of the interstitial carbon atoms.

3.2. Mechanical characterisation

Regarding the mechanical characterisation of the scaffolds, uniaxial compression tests were performed to evaluate their behaviour under compressive stresses, caused by a force applied perpendicular to the building plane of each specimen, which is known to be the weakest orientation in DLP-manufactured structures [36,37]. Representative stress (σ) – strain (ε) curves resulting from these compression tests performed on *CSA*, *RSA* as well as *pl-SPS* specimens sintered at 1200, 1300, 1400 and 1500 °C are included in Fig. 6(a-d). The results in these plots indicate that all specimens, as typical brittle open scaffolds, exhibit a catastrophic failure with several cracking events evidenced by a serrated curve. This performance matches previous reports regarding the mechanical performance of laminated materials subjected to compression stresses in perpendicular configuration [36,37].

The multiple cracking after peak load are to be expected, especially in porous structures, since the initial cracking event does not completely destroy the whole sample and the remaining pieces can still withstand some load. However, cracking events prior to peak load typically indicate the presence of defects which fail prematurely compared to the healthy structure, or to uneven contact with the loading plates. At lower sintering temperatures, such cracking events are attributed mostly to surface defects related to layer attachment which seemed to be reduced at higher sintering temperatures when a greater densification is achieved (Fig. 2). Instead, at higher temperatures, such multiple cracking could be linked to the observed fissures (Fig. 3) generated during phase transformations. Thus, curves corresponding to *RSA* and especially *CSA* specimens generally show multiple local cracks before and after the maximum stress is reached. This is much less common in *pl-SPS* scaffolds, which tend to have a more defined peak stress, generally corresponding to the first peak of the curve, in good agreement with the lower number of fissures observed in their microstructure (Fig. 3).

Average compressive strengths (σ_c) of all sintered scaffolds, as shown in Fig. 7, were within or above the range of strength values for cancellous bone [38]. As expected, the compressive strength of the *pl-SPS* sintered scaffolds increased monotonically with the sintering temperature, in a fairly good correlation with the evolution of their densification (Fig. 4a). A similar tendency was observed for the *CSA* and *RSA* treated scaffolds at the lower temperatures, but their strength suffered a drop upon reaching the highest temperatures. For *CSA* scaffolds, the differences in compressive strength between 1200 and 1400 °C were small and not statistically significant ($p > 0.05$) given the large error bars. Only the strength of scaffolds sintered at 1500 °C is significantly lower due to significantly different microstructure and composition (almost pure α-TCP) and the higher presence of cracks associated with the phase transformation. The increase in strength with temperature from 1200 °C to 1300 °C was most pronounced for the *RSA* scaffolds, with the *RSA-1300* scaffolds exhibiting the highest average compressive strength measured (22 ± 4 MPa), nearly triple the value at 1200 °C (8 ± 3 MPa). However, despite the *RSA-1300* scaffolds relatively fine microstructure and low microporosity (Fig. 4), their strength results still exhibited significant scattering and relatively large error bars. This could be attributed to the appearance of microcracks arising from the phase transformation, but could also be related to some external deformations suffered during densification (Fig. 2). As can be seen in Fig. 5, the number of cracks became more significant at higher sintering temperatures, which explains the drastic drop in *RSA* scaffolds strength down to as low as 4 ± 1 MPa for the *RSA-1500* specimens. The fact that the strengths of the *RSA* specimens at 1200 °C, 1400 °C and 1500 °C fall below those of the *CSA* scaffolds may indicate that the rapid cooling rate causes a build-up of internal residual stresses in the material which is detrimental to its mechanical performance.

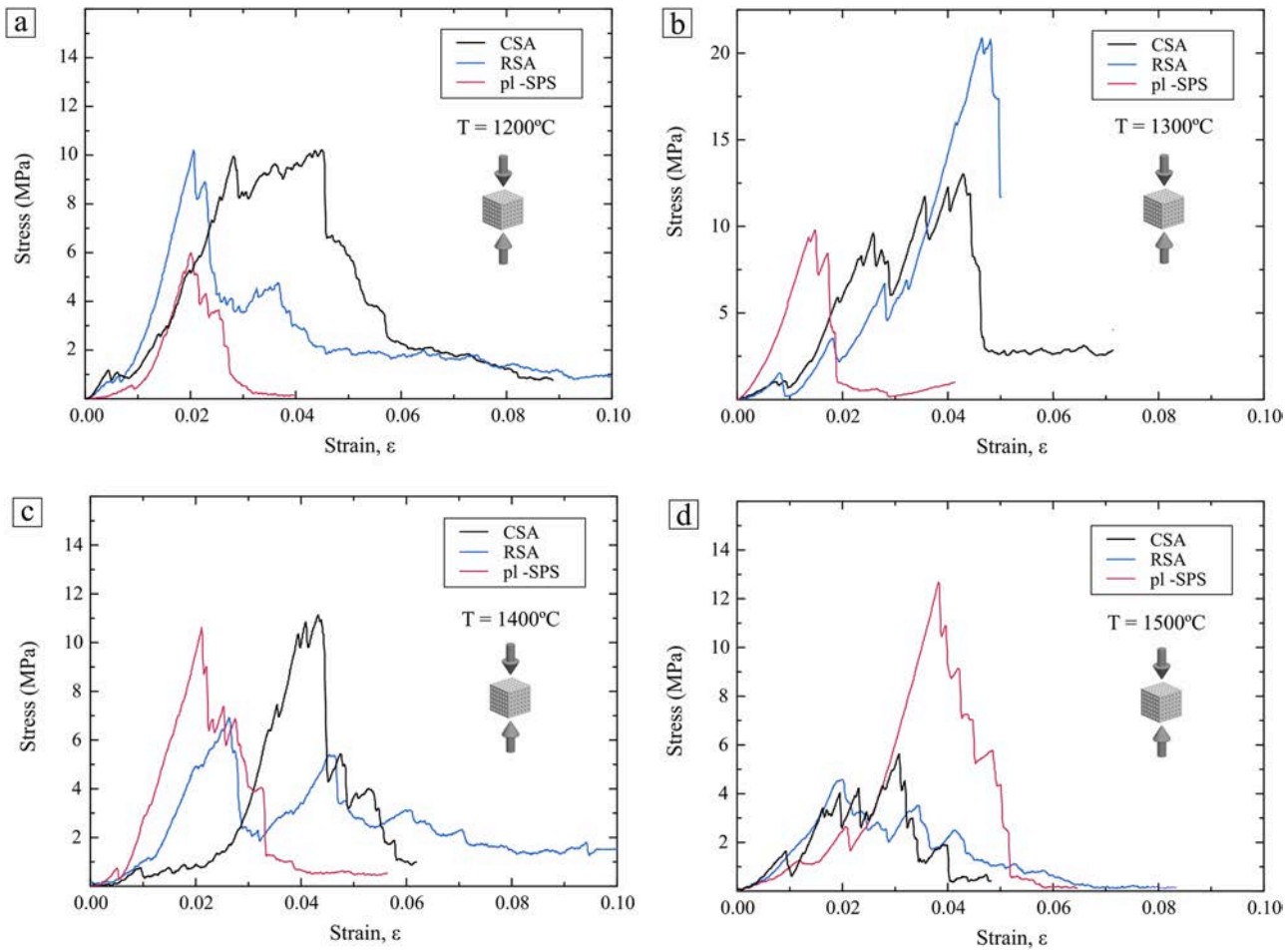

Fig. 6. Representative compressive stress-strain curves of CSA, RSA and pl-SPS scaffolds sintered at (a) 1200 °C, (b) 1300 °C, (c) 1400 °C and (d) 1500 °C, as indicated.

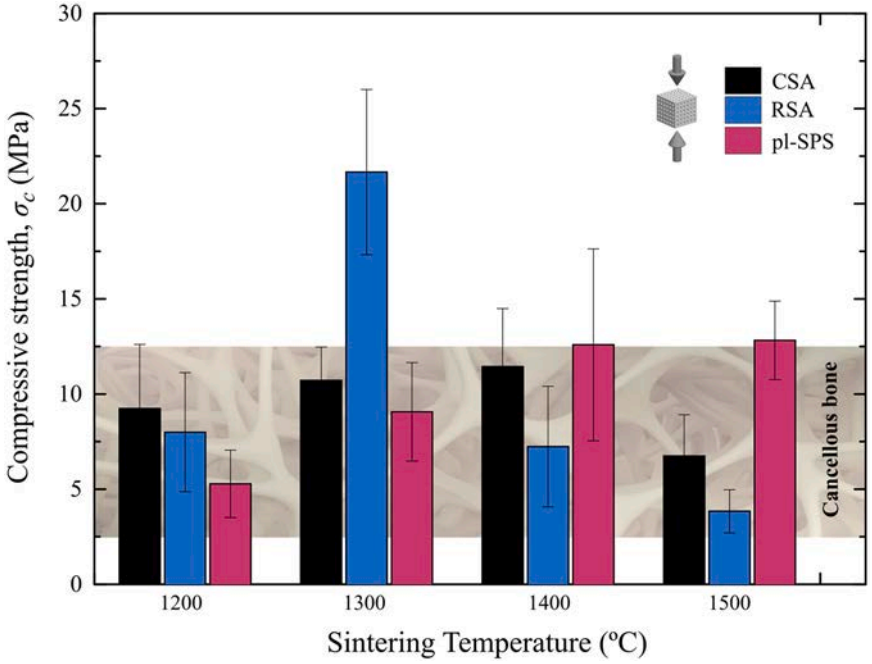

Fig. 7. Average uniaxial compressive strength (with standard deviations as error bars) of scaffolds sintered as indicated in the legend.

Although, as already discussed, the phase transformation to α-TCP is enhanced in *pl-SPS* treated scaffolds when sintered at temperatures above 1300 °C (see Fig. 5), this transformation does not imply a greater presence of cracks in the microstructure (Fig. 3). Accordingly, the highest strength value for this type of scaffolds was measured at the highest temperature of 1500 °C. In particular, the average compressive strength increased progressively from 5 ± 2 MPa at 1200 °C to 13 ± 2 MPa at 1500 °C. In addition, scaffolds sintered in SPS suffered a lower shrinkage and therefore a visibly lower external deformation (Fig. 2). It is presumable that the occurrence of the β→α phase transformation in still relatively porous scaffolds helped to prevent the cracking observed in *CSA* and *RSA* treated scaffolds. Moreover, due to the incorporation of interstitial carbon, the α-phase in the *pl-SPS* scaffolds was stabilised at a much lower sintering temperature (the *SPS-1400* scaffolds already consist of 95% of α-TCP, see Fig. 4), thus avoiding the generation of further cracks even during the reverse α→β transformation. These results suggest that with further optimisation of the heat treatment, it may be possible to obtain dense and crack-free pure α-TCP structures with a good mechanical performance by using *pl-SPS*.

4. Conclusions

Bone scaffolds were fabricated via digital light processing using β-TCP powder as the starting material. Vacuum debinding was followed by sintering, using either conventional furnace, rapid furnace, or pressure-less spark plasma sintering at four different temperatures: 1200, 1300, 1400 and 1500 ºC. Although all three sintering techniques were suitable for densifying the laminated scaffolds, the results varied in terms of composition, microstructure, and mechanical properties:

- Regarding their chemical composition, a certain amount of α-TCP was found in the rapidly sintered scaffolds already at 1300 °C; and in the case of *pl-SPS* scaffolds, the transformation was almost complete at 1400 °C. The results confirm, on the one hand, the need for long dwell times or high temperatures to achieve a complete β→α transformation and, on the other hand, that rapid cooling rates facilitate the retention of the high-temperature phase by avoiding the reverse transformation (α→β). Moreover, the presence of graphite in the sintering chamber plays a crucial role in stabilising the phase, explaining the compositional results obtained in *pl-SPS* scaffolds.

- Regarding their microstructure, the phase transformation and the associated internal stresses caused cracks in the scaffolds, especially when high densifications were reached (e.g., in the *CSA* and *RSA* scaffolds sintered above 1300 ºC). On the other hand, the presence of graphite in the SPS apparatus hindered the densification of scaffolds, whose porosity remained relatively high at all temperatures, but also helped to avoid phase transformation-induced cracks.

- As expected, the average grain sizes of the scaffolds sintered using rapid sintering techniques were significantly smaller than those sintered in a conventional furnace, especially for the *pl-SPS* specimens. In general, while the grain size of *pl-SPS* scaffolds remained almost constant (despite the phase transformation), the size of β-TCP grains present in *RSA* and especially in *CSA* scaffolds increased notably with the sintering temperature. The phase transformation caused a significant reduction in the average grain size in both types of samples, since the α-TCP phase exhibited a very fine (submicrometric) microstructure, with very little tendency to grow with sintering temperature (at least under *pl-SPS* conditions).
- Although all scaffolds exhibited a compressive strength within the range of cancellous bone strength values, their mechanical performance was limited by the presence of cracks, large grains and/or porosity. Interestingly, the presence of α-TCP did not appear to have a negative effect on the compressive strength of the scaffolds. In fact, the pure α-TCP *SPS-1500* scaffolds exhibited the highest strength of all *pl-SPS* sintered scaffolds, and were also the most reliable (lowest relative data scatter) group of scaffolds. Their strength was only surpassed by *RSA-1300* scaffolds, whose struts had a porosity ~43% lower.
- The *RSA-1300* scaffolds were ~ 40% stronger than the best *SPS* specimen and ~50% stronger than the best *CSA* specimen. However, the cracks already present in these scaffolds prevented them from exhibiting a higher strength and their multiplication thwarted efforts to achieve better mechanical performance by increasing the sintering temperature. Similarly, the compressive strength of the *CSA* scaffolds did not quite follow the increase in densification with increasing sintering temperature and was drastically reduced at 1500 ºC by phase transformation-induced cracks.

Although *RSA* has proven to be a suitable technology for obtaining high-density scaffolds that prevent excessive grain growth, and the results obtained with *RSA-1300* samples are promising, in order to obtain more reliable and stronger scaffolds it would be necessary to avoid the generation of phase transformation-induced cracks. The present work provides interesting insights into how the β↔α phase transformation of TCP can be influenced by controlling the heating and cooling rates, as well as dwell time and sintering environment. All this information should prove very useful in designing novel sintering strategies, such as two or multi-step sintering, which could help to improve the already promising *RSA* treatments. In addition, further research investigating the performance of pure α-TCP crack-free *pl-SPS* scaffolds with improved densification and more extensive mechanical analysis, including their performance under bending stresses, may also yield interesting results.

Declaration of Competing Interest

The authors declare that they have no known competing financial interests or personal relationships that could have appeared to influence the work reported in this paper.

Acknowledgements

CzechNanoLab project LM2018110 funded by MEYS CR is gratefully acknowledged for the financial support of the measurements/sample fabrication at CEITEC Nano Research Infrastructure. Similarly, ENAMEL project (PID2021-123218OB-I00) funded by Ministerio de Ciencia e Innovación, Agencia Estatal de Investigación and European Regional Development Fund (MCIN/AEI/10.13039/501100011033/FEDER, UE) is gratefully acknowledged for the financial support of the measurements and sample preparations performed at University of Extremadura. Claudia Paredes acknowledges support from the Spanish Ministerio de Universidades through the programme Margarita Salas para la Formación de Jóvenes Doctores (MS-2), co-funded by the Next Generation EU Funds.

References

[1] J. Jeong, J.H. Kim, J.H. Shim, N.S. Hwang, C.Y. Heo, Bioactive calcium phosphate materials and applications in bone regeneration, Biomater. Res. 23 (2019), https://doi.org/10.1186/s40824-018-0149-3.
[2] I.S. Cho, H.S. Ryu, J.R. Kim, D.W. Kim, K.S. Hong, Sintering behavior and microwave dielectric properties of tricalcium phosphate polymorphs, Jpn. J. Appl. Phys. Part 1 Regul. Pap. Short. Notes Rev. Pap. 46 (2007) 2999–3003, https://doi.org/10.1143/JJAP.46.2999.
[3] A. Barba, A. Diez-Escudero, Y. Maazouz, K. Rappe, M. Espanol, E.B. Montufar, M. Bonany, J.M. Sadowska, J. Guillem-Marti, C. Öhman-Mägi, C. Persson, M. C. Manzanares, J. Franch, M.P. Ginebra, Osteoinduction by foamed and 3D-printed calcium phosphate scaffolds: effect of nanostructure and pore architecture, ACS Appl. Mater. Interfaces 9 (2017) 41722–41736, https://doi.org/10.1021/acsami.7b14175.
[4] I.Y. Kim, J. Wen, C. Ohtsuki, Fabrication of α-tricalcium phosphate ceramics through two-step sintering, Key Eng. Mater. 631 (2014) 78–82, https://doi.org/10.4028/www.scientific.net/kem.631.78.

[5] P. Miranda, A. Pajares, E. Saiz, A.P. Tomsia, F. Guiberteau, Mechanical properties of calcium phosphate scaffolds fabricated by robocasting, J. Biomed. Mater. Res. Part A 85 (2008) 218–227, https://doi.org/10.1002/jbm.a.31587.
[6] Y. Zeng, Y. Yan, H. Yan, C. Liu, P. Li, P. Dong, Y. Zhao, J. Chen, 3D printing of hydroxyapatite scaffolds with good mechanical and biocompatible properties by digital light processing, J. Mater. Sci. 53 (2018) 6291–6301, https://doi.org/10.1007/s10853-018-1992-2.
[7] Y. Lakhdar, C. Tuck, J. Binner, A. Terry, R. Goodridge, Additive manufacturing of advanced ceramic materials, Prog. Mater. Sci. 116 (2021), https://doi.org/10.1016/j.pmatsci.2020.100736.
[8] N. Travitzky, A. Bonet, B. Dermeik, T. Fey, I. Filbert-Demut, L. Schlier, T. Schlordt, P. Greil, Additive manufacturing of ceramic-based materials, Adv. Eng. Mater. (2014) 729–754, https://doi.org/10.1002/adem.201400097.
[9] ASTM International. ASTM F2792–12A, Standard Terminology for Additive Manufacturing Technologies, 2012, https://doi.org/10.1520/F2792-12A.
[10] A. Indurkar, R. Choudhary, K. Rubenis, J. Locs, Advances in sintering techniques for calcium phosphates ceramics, Materials 14 (2021) 1–18, https://doi.org/10.3390/ma14206133.
[11] F.H. Perera, F.J. Martínez-Vázquez, P. Miranda, A.L. Ortiz, A. Pajares, Clarifying the effect of sintering conditions on the microstructure and mechanical properties of β-tricalcium phosphate, Ceram. Int. 36 (2010) 1929–1935, https://doi.org/10.1016/j.ceramint.2010.03.015.
[12] D. Grossin, S. Rollin-Martinet, C. Estournès, F. Rossignol, E. Champion, C. Combes, C. Rey, C. Geoffroy, C. Drouet, Biomimetic apatite sintered at very low temperature by spark plasma sintering: physico-chemistry and microstructure aspects, Acta Biomater. 6 (2010) 577–585, https://doi.org/10.1016/j.actbio.2009.08.021.
[13] D. Kawagoe, K. Ioku, H. Fujimori, S. Goto, Transparent β-tricalcium phosphate ceramics prepared by spark plasma sintering, J. Ceram. Soc. Jpn. 112 (2004) 462–463, https://doi.org/10.2109/jcersj.112.462.
[14] B. Mirhadi, Microwave sintering of nano size powder β-TCP bioceramics, Sci. Sinter. 46 (2014) 185–193, https://doi.org/10.2298/SOS1402185M.
[15] C. Paredes, J. Roleček, L. Pejchalová, P. Miranda, D. Salamon, Impact of residual carbon after DLP and SPS-Sintering on compressive strength and in-VITRO bioactivity of calcium phosphate scaffolds, Open Ceram. 11 (2022), 100281, https://doi.org/10.1016/j.oceram.2022.100281.
[16] C.V. Adake, P. Bhargava, P. Gandhi, Effect of surfactant on dispersion of alumina in photopolymerizable monomers and their UV curing behavior for microstereolithography, Ceram. Int. 41 (2015) 5301–5308, https://doi.org/10.1016/j.ceramint.2014.12.066.
[17] K. Li, Z. Zhao, The effect of the surfactants on the formulation of UV-curable SLA alumina suspension, Ceram. Int. 43 (2017) 4761–4767, https://doi.org/10.1016/j.ceramint.2016.11.143.
[18] Y.H. Lee, J. Bin Lee, W.Y. Maeng, Y.H. Koh, H.E. Kim, Photocurable ceramic slurry using solid camphor as novel diluent for conventional digital light processing (DLP) process, J. Eur. Ceram. Soc. 39 (2019) 4358–4365, https://doi.org/10.1016/j.jeurceramsoc.2019.05.069.
[19] V. Tomeckova, J.W. Halloran, Flow behavior of polymerizable ceramic suspensions as function of ceramic volume fraction and temperature, J. Eur. Ceram. Soc. 31 (2011) 2535–2542, https://doi.org/10.1016/j.jeurceramsoc.2011.01.019.
[20] H. Wu, Y. Cheng, W. Liu, R. He, M. Zhou, S. Wu, X. Song, Y. Chen, Effect of the particle size and the debinding process on the density of alumina ceramics fabricated by 3D printing based on stereolithography, Ceram. Int. 42 (2016) 17290–17294, https://doi.org/10.1016/j.ceramint.2016.08.024.
[21] M. Zhou, W. Liu, H. Wu, X. Song, Y. Chen, L. Cheng, F. He, S. Chen, S. Wu, Preparation of a defect-free alumina cutting tool via additive manufacturing based on stereolithography – optimization of the drying and debinding processes, Ceram. Int. 42 (2016) 11598–11602, https://doi.org/10.1016/j.ceramint.2016.04.050.
[22] E. Champion, Sintering of calcium phosphate bioceramics, Acta Biomater. 9 (2013) 5855–5875, https://doi.org/10.1016/j.actbio.2012.11.029.
[23] D. Bozkurt, M.K. Akarsu, I. Akin, G. Goller, Phase analysis, mechanical properties and in vitro bioactivity of graphene nanoplatelet-reinforced silicon nitride-calcium phosphate composites, J. Asian Ceram. Soc. 9 (2021) 471–486, https://doi.org/10.1080/21870764.2021.1891664.
[24] H.-S. Ryu, H.-J. Youn, K.S. Hong, B.-S. Chang, C.-K. Lee, S.-S. Chung, An Improvement in Sintering Property of B-tricalcium Phosphate by Addition of Calcium Pyrophosphate, 2002.
[25] L. Lutterotti, S. Matthies, H.R. Wenk, MAUD: A Friendly Java Program for Material Analysis Using Diffraction, 1999.
[26] M. Mathew, L.W. Schroeder, B. Dickens, W.E. Brown, The crystal structure of [alpha]-Ca3(PO4)2, Acta Crystallogr. Sect. B 33 (1977) 1325–1333, https://doi.org/10.1107/S0567740877006037.
[27] M. Yashima, A. Sakai, T. Kamiyama, A. Hoshikawa, Crystal structure analysis of β-tricalcium phosphate Ca 3(PO4)2 by neutron powder diffraction, J. Solid State Chem. 175 (2003) 272–277, https://doi.org/10.1016/S0022-4596(03)00279-2.
[28] S. Graulis, D. Chateigner, R.T. Downs, A.F.T. Yokochi, M. Quirós, L. Lutterotti, E. Manakova, J. Butkus, P. Moeck, A. Le Bail, Crystallography open database - an open-access collection of crystal structures, J. Appl. Crystallogr 42 (2009) 726–729, https://doi.org/10.1107/S0021889809016690.
[29] P. Miranda, E. Saiz, K. Gryn, A.P. Tomsia, Sintering and robocasting of β-tricalcium phosphate scaffolds for orthopaedic applications, Acta Biomater. 2 (2006) 457–466, https://doi.org/10.1016/j.actbio.2006.02.004.
[30] K. Morita, B.N. Kim, H. Yoshida, K. Hiraga, Y. Sakka, Distribution of carbon contamination in oxide ceramics occurring during spark-plasma-sintering (SPS) processing: II - effect of SPS and loading temperatures, J. Eur. Ceram. Soc. 38 (2018) 2596–2604, https://doi.org/10.1016/j.jeurceramsoc.2017.12.004.
[31] S. Hříbalová, W. Pabst, Theoretical study of the influence of carbon contamination on the transparency of spinel ceramics prepared by spark plasma sintering (SPS), J. Eur. Ceram. Soc. 41 (2021) 4337–4342, https://doi.org/10.1016/j.jeurceramsoc.2021.01.036.
[32] M. Bohner, B.L.G. Santoni, N. Döbelin, β-tricalcium phosphate for bone substitution: synthesis and properties, Acta Biomater. 113 (2020) 23–41, https://doi.org/10.1016/j.actbio.2020.06.022.
[33] D. Brazete, P.M.C. Torres, J.C.C. Abrantes, J.M.F. Ferreira, Influence of the Ca/P ratio and cooling rate on the allotropic α↔β-tricalcium phosphate phase transformations, Ceram. Int. 44 (2018) 8249–8256, https://doi.org/10.1016/j.ceramint.2018.02.005.
[34] R.G. Carrodeguas, A.H. De Aza, X. Turrillas, P. Pena, S. De Aza, New approach to the β→α polymorphic transformation in magnesium-substituted tricalcium phosphate and its practical implications, J. Am. Ceram. Soc. 91 (2008) 1281–1286, https://doi.org/10.1111/j.1551-2916.2008.02294.x.
[35] R.G. Carrodeguas, S. De Aza, α-Tricalcium phosphate: synthesis, properties and biomedical applications, Acta Biomater. 7 (2011) 3536–3546, https://doi.org/10.1016/j.actbio.2011.06.019.
[36] P. Feng, X. Meng, J.F. Chen, L. Ye, Mechanical properties of structures 3D printed with cementitious powders, Constr. Build. Mater. 93 (2015) 486–497, https://doi.org/10.1016/j.conbuildmat.2015.05.132.
[37] C. Paredes, F.J. Martínez-Vázquez, H. Elsayed, P. Colombo, A. Pajares, P. Miranda, Evaluation of direct light processing for the fabrication of bioactive ceramic scaffolds: effect of pore/strut size on manufacturability and mechanical performance, J. Eur. Ceram. Soc. 41 (2021) 892–900, https://doi.org/10.1016/j.jeurceramsoc.2020.09.002.
[38] L.L. Hench, 8 – The skeletal system, in: L.L. Hench, J.R. Jones (Eds.), Biomaterials, Artificial Organs and Tissue Engineering, Woodhead Publishing, 2005, pp. 79–89, https://doi.org/10.1533/9781845690861.2.79.